
ENERGY CONSUMPTION OF GEO-TO-GROUND BEACONLESS LINK ACQUISITION AGAINST RANDOM VIBRATION WITH COHERENT DETECTION

A PREPRINT

✉ **Sen Yang**

School of Astronautics and Aeronautics
University of Electronic Science and Technology of China
Chengdu, China 611731
yang_jansen@163.com

✉ **Xiaofeng Li**

School of Astronautics and Aeronautics
University of Electronic Science and Technology of China
Chengdu, China 611731
lxf3203433@uestc.edu.cn

December 20, 2024

ABSTRACT

The GEO satellite maintains good synchronization with the ground, reducing the priority of acquisition time in the establishment of the optical link. Whereas energy is an important resource for the satellite to execute space missions, the consumption during the acquisition process rises to the primary optimization objective. However, no previous studies have addressed this issue. Motivated by this gap, this paper first model the relationship between the transmitted power and the received SNR in the coherent detection system, with the corresponding single-field acquisition probability, the acquisition time is then calculated, and the closed-form expression of the multi-field acquisition energy consumption is further derived in scan-stare mode. Then for dual-scan technique, through the induction of the probability density function of acquisition energy, it is transformed into the equivalent form of scan-stare, thereby acquiring acquisition energy. Subsequently, optimizations are performed on these two modes. The above theoretical derivations are verified through Monte Carlo simulations. Consequently, the acquisition energy of dual-scan is lower than that of scan-stare, with the acquisition time being about half of the latter, making it a more efficient technique. Notably, the optimum beam divergence angle is the minimum that the laser can modulate, and the beaconless acquisition energy is only 6% of that with the beacon, indicating that the beaconless is a better strategy for optical link acquisition with the goal of energy consumption optimization.

Keywords Optical Link Acquisition · Coherent Detection · Platform Vibration · Multi-field Energy Consumption · Optimizations

The incorporation of big data in satellite communication has raised bandwidth demands of over 10 Gbps. Microwave communication systems are no longer sustainable in high-speed communication due to their low bandwidth magnitude and slow modulation rate Toyoshima et al. [2007]. In contrast, free-space optics communication (FSOC) can effectively be implemented as it provides several benefits, including a vast bandwidth, license-free spectrum, low power consumption, and minimal space requirements Toyoshima [2005]. As a result, numerous satellite-to-ground laser communication verification missions have gained significant success to date. From the LEO-to-ground laser communication experiment of STRV-2 module in 2000 Kim et al. [2001]. Then the first high data rate (5.625 Gbps) bidirectional link using 1064nm coherent waveform between the NFIRE satellite and the optical ground station in 2010 Fields et al. [2011]. To current routine high-performance inter-satellite links between the Alphasat on GEO and the Sentinel-1A/1B on LEO Benzi et al.

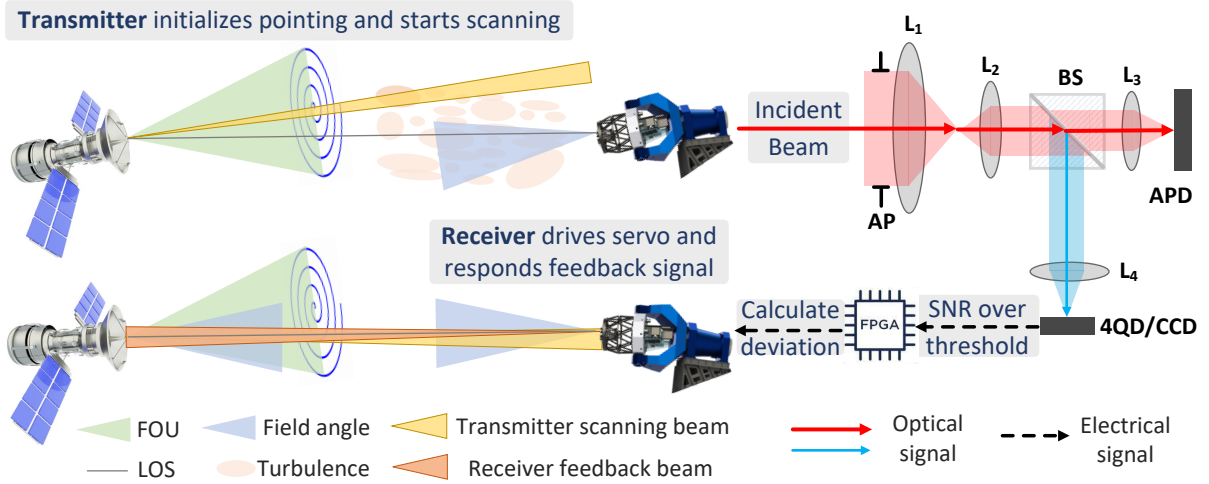


Figure 1: The diagram of beaconless acquisition. There is an error between the initial pointing and the LoS. The green conical covers the LoS so that the beam can propagate to the receiver antenna by scanning. Analogously, the field of view in blue conical covers LoS so that the received photons of the signal beam can fall on the photoelectric sensor. The incident beam passes through an AP and is then expanded by the telescope system $L_1 - L_2$. It subsequently passes through a BS and most of it is focused on an APD through L_3 for signal processing. The remaining small portion of the beam is detected by a 4QD or CCD through L_4 for spot deviation measurement. L_1, L_2, L_3, L_4 , lens; AP, aperture; BS, beam splitter; APD, avalanche photo diode; 4QD, four-quadrant detector; CCD, charge-coupled device photodetector.

[2016]. And the future EDRS provides global coverage for fast data transmission between network nodes and offers long-distance secure point-to-point communication Hauschildt et al. [2019].

The crucial step for establishing FSOC is optical link acquisition Young et al. [1986], which has also been employed in precision measurement missions, such as GRACE FOWuchenich et al. [2014] for Earth gravitational field measurement, as well as LISABarausse et al. [2020] and TAIJI program Luo et al. [2021] for space gravitational wave observation. Herein, we provide a typical optical link acquisition process to refine the background information Guelman et al. [2004]. The transmitted and the received terminals on both sides of the optical link are defined as T1 and T2, respectively. Firstly, T1 and T2 utilize an ephemeris table for initial pointing. Due to differences in attitude and ephemeris, as well as thermal deformation and other factors, there is a certain angular deviation between the initial pointing and the line-of-sight (LoS), which is distributed randomly Toyoshima et al. [2002], resulting in uncertainty for beam pointing. Then T1 performs a scanning with the Archimedes spiral Steinhaus [1999] to cover the field of uncertainty (FOU) of T2, while T2 maintains a staring posture. When T2 receives a laser signal with sufficient intensity, the distortion of spot on photodetector is corrected with adaptive optics Yang and Li [2022a,b], the deviation of the spot is calculated Fu et al. [2021], Qiu et al. [2021] and the pointing is adjusted slightly so that the spot moves to the center of the photodetector. Subsequently, T2 feeds back the optical signal. After the response of the photodetector of T1 is triggered, T1 stops scanning and the acquisition is completed The diagram is illustrated in Fig. 1.

However, the advantage of good security brought by the smaller beamwidth has been proven to be a major drawback in the establishment of an optical link. Some studies adopted the beacon acquisition mode, where a wide beacon beam with sufficient peak power is used for scanning initially, followed by switching to a narrow beam for precise tracking when the two terminals are basically aligned. Yu et al. [2017] studies the constraint boundary conditions for acquiring the beacon from the perspective of theory and experiment. A multi-parameter influenced pointing jitter error structure for the low orbit communication experimental satellite system has been established in Hu et al. [2022]. However, in addition to the signal light laser, this system also requires a beacon laser device, which is not conducive to the miniaturization design of the system.

Ref. Hindman and Robertson [2004] proposed a beaconless acquisition method that achieves scanning acquisition and LoS correction solely with the use of a narrow signal beam. Compared to the classical beacon, the beaconless method simplifies the terminal structure and reduces power requirements, while maintaining performance levels. However, the acquisition process poses significant challenges due to the narrow beam divergence angle and random vibration

disturbanceHo [2007]. To address these challenges, analytic expressions and optimizations for multi-scan average acquisition time were presented inLi et al. [2011]. In addition, an approximate mathematical model investigating the influence of Gaussian random vibration on the acquisition probability was proposed inFriederichs et al. [2016]. Ref.Ma et al. [2021] derived an approximate analytical expression for the scan loss probability with platform vibration, whose influence on acquisition time was analyzed under both single-field and multi-field scanning scenarios. Furthermore, Ref.Hechenblaikner [2021] assessed the probability of failing to acquire a link due to beam jitter and derived a simple analytical model that allowed determining the maximum tolerable jitter for a given beam overlap and required probability of success. These models assumed that the scanning beam was detected with a sufficiently high signal-to-noise ratio (SNR). However, the actual transmitted power is limited and will also be affected by turbulenceKaushal and Kaddoum [2016] and link losses, resulting in a significant attenuation of the power incident on the photodetector of the receiver. Moreover, there is noise output caused by dark current or other factors on the sensorsLi [2015], making the receiver SNR an important parameter that cannot be ignored.

The GEO satellite maintains good synchronization with the ground, and its satellite-to-ground communication window is wide. Hence, the establishment of the GEO-to-ground optical link does not impose stringent requirements on acquisition time. Rather, optimizing energy consumption, a crucial resource for satellites to execute space missionsChin et al. [2018], Cui et al. [2023], should be the primary objective in the acquisition process. Nevertheless, to the best of our knowledge, there is no work has yet studied on it. Spurred by this gap, this paper provides detailed studies and discussions on the modeling and optimization of energy consumption for GEO-to-ground optical link acquisition. Considering the combined effects of platform vibration following the Rice distribution and atmospheric turbulence obeying the Gamma-Gamma distribution, we first model the transmitted power under a given average SNR at the receiver. Then, with the corresponding single-field acquisition probability, the probability density function (PDF) of multi-field acquisition time is derived. By integrating these components, the closed-form expression of the acquisition energy consumption is obtained in the scan-stare mode. Additionally, we conduct parameter optimizations for spiral pitch, beam divergence angle, coverage factor, and FOU. For the dual-scan mode, it is treated as two independent scan-stare processes. Subsequently, the PDF of multi-field acquisition energy consumption is derived and generalized to an equivalent scan-stare form, which enables to derive the expectation of multi-field acquisition energy consumption, and carry out optimizations. Finally, the Monte Carlo (MC) simulations also including the analysis of platform vibration and scanning speed are performed.

The structure of the remaining sections of this article is as follows: Chapter 2 presents the model for transmitted power. Chapter 3 computes the energy consumption expectation for single-field acquisition. Building on this, Chapter 4 derives the energy consumption expectation for multi-field acquisition in both scan-stare and dual-scan modes, and performs optimization of acquisition parameters. Chapter 5 validates the theoretical derivations and optimization conclusions through MC simulations. Lastly, Chapter 6 offers a summary of the paper.

1 Power Model

The average SNR of FSOC system isAndrews and Phillips [2005]:

$$\bar{Q} = \langle i_s^2 \rangle / \langle i_n^2 \rangle \quad (1)$$

where i_s is signal current. i_n is noise current, which is additive Gaussian white noise with zero mean and $\sigma_n^2 = N_0$ variance. Due to the long transmission distance of GEO-to-ground laser communication, it is difficult to meet the demand of high communication rate by direct detectionPopoola et al. [2012] under the condition of limited power. In contrast, the coherent detection offers advantages such as high receiver sensitivity, high communication rates, and strong resistance to background light interference. Consequently, in the coherent detection system, the photocurrent output by the balanced detector isPeppas and Mathiopoulos [2015]:

$$i_s = 2\sqrt{P_r P_L} R_r \cos(\Delta w \cdot t + \Delta\phi) \quad (2)$$

where $P_r = P_t h_t h_c$, P_t and P_r are the transmitter and receiver powers, respectively, h_t represents the transmission gain with vibration, h_c represents the turbulence attenuation, the two are independentJurado-Navas et al. [2012]. R_r is the photoelectric response efficiency, P_L is the local oscillator power, Δw is the frequency difference between the signal and the local oscillator light, and $\Delta\phi$ is the phase difference between the signal and the local oscillator light. Therefore, the Eq. (1) is expressed as:

$$\bar{Q} = 2P_t P_L R_r^2 E[h_t] E[h_c] / N_0 \quad (3)$$

h_t denotes the ratio of received power to transmitted power in the absence of turbulence, which can be derived from Gaussian beam diffraction propagation as follows:

$$h_t(\varphi) = \frac{2s_t s_r s_s}{\pi R^2} \frac{1}{\omega^2} \exp\left(-\frac{2\varphi^2}{\omega^2}\right) \cdot \pi \left(\frac{D_r}{2}\right)^2 \quad (4)$$

where R is the far-field propagation distance, s_t and s_r are the transmitted and received loss, respectively, s_s is the proportion of split beam for acquisition, D_r is the diameter of the receiver aperture, ω is divergence angle corresponding to $1/e^2$ intensity radius of Gaussian beam. φ represents the random variable denoting the deviation angle between the transmitter pointing and the LoS under the influence of vibration, as illustrated in Fig. 2. Ref. [13] has previously demonstrated that φ follows a Rice distribution. Hence, $E[h_t]$ is obtained as:

$$\begin{aligned} E[h_t] &= \frac{s_t s_r s_s D_r^2}{2R^2} E_\varphi \left[\frac{1}{\omega^2} \exp\left(-\frac{2\varphi^2}{\omega^2}\right) \right] \\ &= \frac{s_t s_r s_s D_r^2}{2R^2} \frac{1}{\omega^2 + 4\sigma^2} \exp\left(-\frac{2\tau^2 d^2}{\omega^2 + 4\sigma^2}\right) \end{aligned} \quad (5)$$

where d is the distance between adjacent spiral arms, denoted as spiral pitch, σ is the standard deviation of the platform vibration. Notably, $0 \leq \tau \leq 1/2$ is coverage factor, representing the ratio of maximum acquisition angle to spiral pitch where the receiver meets lowest SNR level for a certain transmitted power. When the minimum distance between spirals and the receiver exceeds τd , it implies that the received average SNR consistently falls below the threshold, resulting in acquisition failure.

The atmospheric turbulence is modeled by the Gamma-Gamma distribution Al-Habash et al. [2001]. Then the first moment of h_c is given as Wang and Cheng [2010]:

$$E[h_c] = \frac{\Gamma(\alpha + k)\Gamma(\beta + 1)}{\Gamma(\alpha)\Gamma(\beta)} \left(\frac{\gamma}{\alpha\beta}\right) = \gamma \quad (6)$$

where γ is the scale parameter, α and β are large-scale and small-scale effective numbers Prokeš [2009], respectively.

Combining Eqs. (3), (5) and (6), the transmitted power P_t meeting the average SNR threshold at the receiver is derived as:

$$P_t = B (\omega^2 + 4\sigma^2) \exp\left(\frac{2\tau^2 d^2}{\omega^2 + 4\sigma^2}\right) \quad (7)$$

where $B = \frac{\bar{Q} N_0 R^2}{P_L R_s^2 s_t s_r s_s \gamma D_r^2}$.

2 Single-field Acquisition Energy

As depicted in scanning process Fig. 2, the polar coordinate of initial pointing error (or the position of the receiver) is (ρ_r, θ_r) , obeying the Gaussian distribution with zero mean and equal variance $\kappa_x = \kappa_y = \kappa$ in the horizontal and vertical directions. So the polar angle θ_r follows uniform distribution $U(0, 2\pi)$ and the radial error ρ_r obeys Rayleigh distribution as:

$$f_{\rho_r}(\rho_r) = \frac{\rho_r}{\kappa^2} \exp\left(-\frac{\rho_r^2}{2\kappa^2}\right) \quad (8)$$

The receiver (ρ_r, θ_r) is likely to be scanned within the FOU, and the corresponding probability is expressed as:

$$P_U = \int_0^U f_{\rho_r}(\rho_r) d\rho_r = 1 - \exp\left(-\frac{U^2}{2\kappa^2}\right) \quad (9)$$

Given that κ , measured in milliradian magnitude, is significantly far greater than d in microradian magnitude, the PDF of the coverage factor τ is approximated as:

$$\begin{aligned} f_\tau(\tau) &\approx \sum_{k=1}^{\infty} \left[\exp\left(-\frac{(k-1+\tau)^2 d^2}{2\kappa^2}\right) - \exp\left(-\frac{(k+\tau)^2 d^2}{2\kappa^2}\right) \right. \\ &\quad \left. - \exp\left(-\frac{(k+1-\tau)^2 d^2}{2\kappa^2}\right) + \exp\left(-\frac{(k-\tau)^2 d^2}{2\kappa^2}\right) \right] \\ &= \exp\left(-\frac{\tau^2 d^2}{2\kappa^2}\right) + \exp\left(-\frac{(1-\tau)^2 d^2}{2\kappa^2}\right) \approx 2 \end{aligned} \quad (10)$$

According to the description in Fig. 2, The probability that the average received SNR over the threshold is the CDF of the coverage factor:

$$P_{SNR} = \int_0^\tau f_\tau(\mathcal{T}) d\mathcal{T} = 2\tau \quad (11)$$

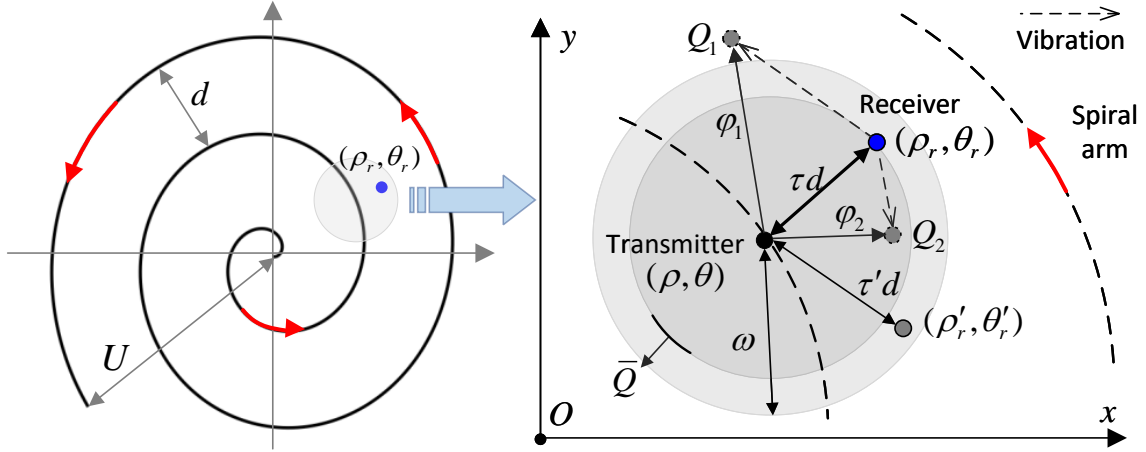


Figure 2: Scanning diagram. U is FOU, d is spiral pitch, and ω is beam divergence angle. Under the platform vibration, φ is the random angle deviation between the transmitter pointing and LoS (the direction pointing towards the receiver). $\mu = \tau d$ is the maximum acquisition angle between spiral arms and receiver meeting the SNR threshold. While $\mu' = \tau' d$ represents an alternative position, but acquisition fails due to $\mu' > \mu$.

In addition, the signal is expected to be detected when the LoS falls within the field angle range of the receiver, and the corresponding field detection probability is denoted as $P_V < 1$. We refer to $P_R = P_V \cdot P_{SNR} = 2P_V\tau$ as the feedback probability of the receiver. Consequently, the probability of successful acquisition in a single-field scanning is:

$$P_S = P_U \cdot P_R \quad (12)$$

As shown in Fig. 2, the scanning usually adopts the Archimedean spiral to achieve an efficient search from high probability to low probability regions Steinhaus [1999]. For the radial distance ρ_r , the length of the spiral scan is $\pi\rho_r^2/d$. Then the acquisition time is calculated as $t_S = \pi\rho_r^2/(vd)$, where v is scanning speed. Combined with Eq. (8), the PDF of single-field acquisition energy consumption $e_S = P_t \cdot t_S$ is obtained as:

$$f_{e_S}(e_S) = \frac{vd}{2\pi\kappa^2 P_t} \exp\left(-\frac{vd}{2\pi\kappa^2 P_t} e_S\right) \quad (13)$$

Subsequently, when a single-field acquisition is successful, the energy consumption expectation E_S is integrated as:

$$E_S = \int_0^{E_U} e_S \cdot f_{e_S}(e_S) de_S = \frac{2\pi\kappa^2 P_t}{vd} \left[1 - \exp\left(-\frac{U^2}{2\kappa^2}\right) \left(1 + \frac{U^2}{2\kappa^2}\right) \right] \quad (14)$$

where $E_U = \pi U^2 P_t / (vd)$ represents the energy consumption of scanning the entire FOU.

3 Multi-field Scanning Model

Acquisition success cannot be guaranteed with only once single-field scanning due to $P_S < 1$. Therefore, the multi-field scanning, which is a series of repetitive single-field scanning over the same FOU, is often employed instead.

3.1 Scan-stare

In the case of a single-field scanning failure, it is necessary to reinitialize the transmitter pointing based on ephemeris table. In this process, reset energy E_a , which is not related to P_t , is strongly essential but ignored by previous analytical models. Therefore, when the acquisition is achieved in $n + 1$ single-field, the total scanning energy e_M is:

$$e_M = n(E_U + E_a) + e_S \quad (15)$$

The PDF of e_M is:

$$f_{e_M}(e_M) = (1 - P_S)^n P_R f_{e_S}(e_S) \quad (16)$$

The CDF of e_M is:

$$\begin{aligned}
P(E \leq e_M) &= P(E \leq n(E_U + E_a)) + P(n(E_U + E_a) < E \leq e_M) \\
&= \sum_{k=0}^{n-1} (1 - P_S)^k P_R \int_0^{E_U} f_{e_S}(E) dE + (1 - P_S)^n P_R \int_0^{e_S} f_{e_S}(E) dE \\
&= 1 - (1 - P_S)^n \left\{ 1 - P_R \left[1 - \exp\left(-\frac{vd}{2\pi\kappa^2 P_t} e_S\right) \right] \right\}
\end{aligned} \tag{17}$$

There is $n \rightarrow \infty$ and $e_S \rightarrow E_U$ for $e_M \rightarrow \infty$. Then the acquisition probability of Eq. (17) becomes:

$$\lim_{e_M \rightarrow \infty} P(E \leq e_M) = \lim_{n \rightarrow \infty} \left[1 - (1 - P_S)^{n+1} \right] = 1 \tag{18}$$

Multi-field scanning can ensure acquisition success from an energy consumption perspective. According to Eq. (16), the multi-field acquisition energy expectation E_M is calculated as:

$$\begin{aligned}
E_M &= \int_0^\infty e_M \cdot f_{e_M}(e_M) de_M = \sum_{n=0}^\infty (1 - P_S)^n P_R \int_0^{E_U} [n(E_U + E_a) + e_S] \cdot f_{e_S}(e_S) de_S \\
&= \sum_{n=0}^\infty (1 - P_S)^n P_S \left[\frac{E_S}{P_U} + n(E_U + E_a) \right] = \frac{E_S}{P_U} + \left(\frac{1}{P_S} - 1 \right) (E_U + E_a) \\
&= \frac{2\pi\kappa^2 P_t}{vd} \left[\frac{e^\eta \eta (1 - P_R)}{(e^\eta - 1) P_R} + 1 \right] + \frac{E_a [e^\eta (1 - P_R) + P_R]}{(e^\eta - 1) P_R}
\end{aligned} \tag{19}$$

where $\eta = U^2/(2\kappa^2) > 0$. Obviously, E_M is a function of the parameters (d, τ, ω, U) , which are optimized respectively to minimize the acquisition energy.

3.1.1 Optimizations

The partial derivative of E_M with respect to d is:

$$\frac{\partial E_M}{\partial d} = \frac{2\pi\kappa^2 P_t}{vd^2 (\omega^2 + 4\sigma^2)} \left[\frac{e^\eta \eta (1 - P_R)}{(e^\eta - 1) P_R} + 1 \right] (4\tau^2 d^2 - \omega^2 - 4\sigma^2) \tag{20}$$

where the minimum is taken at $\partial E_M / \partial d = 0$, with the optimum d_{opt} as:

$$d_{opt} = \frac{\sqrt{\omega^2 + 4\sigma^2}}{2\tau} \tag{21}$$

Substituting it into Eq. (19) yields:

$$E_M|_{d=d_{opt}} = \frac{2\pi e^{1/2} \kappa^2 B}{v(\omega^2 + 4\sigma^2)^{-1/2}} \left[\frac{e^\eta \eta (1 - P_R)}{(e^\eta - 1) P_V} + \frac{P_R}{P_V} \right] + \frac{E_a [e^\eta (1 - P_R) + P_R]}{(e^\eta - 1) P_R} \tag{22}$$

Then take the partial derivative concerning ω :

$$\frac{\partial E_M}{\partial \omega} = \frac{2\pi e^{1/2} \kappa^2 B \omega}{v\sqrt{\omega^2 + 4\sigma^2}} \left[\frac{e^\eta \eta (1 - P_R)}{(e^\eta - 1) P_V} + \frac{P_R}{P_V} \right] \tag{23}$$

which is always greater than zero, so the optimum beam divergence angle ω_{opt} is the lower limit of the divergence angle ω_{limit} that the laser can modulate.

Next, the partial derivative of Eq. (22) with respect to τ is:

$$\frac{\partial E_M}{\partial \tau} = -\frac{4\pi e^{1/2} \kappa^2 B (e^\eta \eta - e^\eta + 1)}{v(\omega^2 + 4\sigma^2)^{-1/2} (e^\eta - 1)} - \frac{E_a e^\eta}{(e^\eta - 1) P_R \tau} \tag{24}$$

where $e^\eta \eta - e^\eta + 1$ is positive constantly. Thus E_M decreases monotonically with τ , and the minimum E_M is reached at $\tau_{opt} = 1/2$.

Furthermore, the partial derivative of E_M concerning η is calculated after taking τ_{opt} into Eq. (22):

$$\frac{\partial E_M}{\partial \eta} = \frac{2\pi e^{1/2} \kappa^2 B (1 - P_V) e^\eta (e^\eta - \eta - 1 - \hat{E}_a)}{v(\omega^2 + 4\sigma^2)^{-1/2} (e^\eta - 1)^2 P_V} \quad (25)$$

where $\hat{E}_a = \frac{v(\omega^2 + 4\sigma^2)^{-1/2} E_a}{2\pi e^{1/2} \kappa^2 B(1 - P_V)}$. The minimum E_M is taken at $\partial E_M / \partial \eta = 0$:

$$e^\eta - \eta - 1 - \hat{E}_a = 0 \quad (26)$$

However, the above equation has no analytical solution. When η is large, there is approximate $\eta \approx \ln(\hat{E}_a)$, which can be employed as the variable to perform polynomial fitting with numerical solutions and effectively reduce the order. In general, ω is 10^{-5} magnitude, v and κ are of the same order of 10^{-3} magnitude, $(1 - P_V)$ and E_a are the level of 10^{-2} and 10^2 , respectively, and B is at 10^7 level. Therefore, \hat{E}_a is about $10^{-1} \sim 10^0$ magnitude order. Without loss of generality, we adopt polynomials to fit the numerical solutions, where the goodness of fit (GoF) is utilized as an index to evaluate the fitting accuracy. We perform piecewise fitting in the interval $[0.01, 10]$ for $x = \ln(\hat{E}_a)$ with $GoF = 0.999$:

$$\eta_{opt} = \begin{cases} 0.02785x^2 + 0.3123x + 0.9870, & 0.01 \leq \hat{E}_a < 0.1 \\ 0.06049x^2 + 0.4552x + 1.1454, & 0.1 \leq \hat{E}_a \leq 1 \\ 0.07181x^2 + 0.4713x + 1.1455, & 1 < \hat{E}_a \leq 10 \end{cases} \quad (27)$$

Consequently, the optimum FOU is $U_{opt} = \kappa \sqrt{2\eta_{opt}}$.

3.2 Dual-scan

In this section, we investigate another type of acquisition process known as the dual-scan. This mode involves two terminals simultaneously performing scan. Once one of the terminals acquires the other, both terminals stop scanning and proceed to the pointing operation. Therefore, the dual-scan process can be visualized as two individual scan-stare procedures.

We assume that the parameters of both terminals are the same. Two independent random variables E_1 and E_2 represent the energy required for T1 to acquire T2 and T2 to acquire T1, respectively. The energy consumption of acquisition first is lower, and the random variable for dual-scan acquisition energy consumption is represented by Hechenblaikner [2021]:

$$E = 2 \cdot \min \{E_1, E_2\} \quad (28)$$

For the energy consumption $\tilde{e}_M = n (\tilde{E}_U + \tilde{E}_a) + \tilde{e}_S$, the CDF is computed as:

$$\begin{aligned} F_{\min}(\tilde{e}_M) &= P_{\min}(E \leq \tilde{e}_M) = 1 - P_{\min}(E > \tilde{e}_M) = 1 - P\left(E_1 > \frac{\tilde{e}_M}{2}\right) \cdot P\left(E_2 > \frac{\tilde{e}_M}{2}\right) \\ &= 1 - (1 - P_S)^{2n} \left\{ 1 - P_R \left[1 - \exp\left(-\frac{vd \left[\tilde{e}_M - n(\tilde{E}_U + \tilde{E}_a)\right]}{2\pi\kappa^2 \tilde{P}_t}\right) \right] \right\}^2 \end{aligned} \quad (29)$$

where $\tilde{E}_U = 2E_U$, $\tilde{E}_a = 2E_a$, and $\tilde{P}_t = 2P_t$. Then we get the corresponding PDF by taking the derivative concerning \tilde{e}_M :

$$f_{\tilde{e}_M}(\tilde{e}_M) = (1 - \tilde{P}_S)^n P_R f_{\tilde{e}_S}(\tilde{e}_S) \quad (30)$$

where $\tilde{P}_S = P_S(2 - P_S)$. Eq. (30) shares a similar expression form with Eq. (16). Consequently, we are able to transform the complex dual-scan into the simpler scan-stare, which has been previously analyzed albeit with distinct parameters. The corresponding PDF of single-field acquisition energy is generalized as:

$$f_{\tilde{e}_S}(\tilde{e}_S) = \frac{vd}{\pi\kappa^2 \tilde{P}_t} \exp\left(-\frac{vd\tilde{e}_S}{\pi\kappa^2 \tilde{P}_t}\right) \left[\exp\left(\frac{vd\tilde{e}_S}{2\pi\kappa^2 \tilde{P}_t}\right) (1 - P_R) + P_R \right] \quad (31)$$

Analogously, the probability \tilde{P}_U of falling within the FOU is:

$$\tilde{P}_U = \int_0^{\tilde{E}_U} f_{\tilde{e}_S}(\tilde{e}_S) d\tilde{e}_S = (1 - e^{-\eta}) (2 - P_R + P_R e^{-\eta}) \quad (32)$$

Then the single-field acquisition energy \tilde{E}_S is obtained as:

$$\begin{aligned}\tilde{E}_S &= \int_0^{\tilde{E}_V} \tilde{e}_S \cdot f_{\tilde{e}_S}(\tilde{e}_S) d\tilde{e}_S \\ &= \frac{\pi \kappa^2 \tilde{P}_t [e^{2\eta} (4 - 3P_R) - 4e^\eta (\eta + 1) (1 - P_R) - P_R (2\eta + 1)]}{vd \cdot e^{2\eta}}\end{aligned}\quad (33)$$

Consequently, the multi-field acquisition energy expectation \tilde{E}_M is calculated:

$$\begin{aligned}\tilde{E}_M &= \frac{\tilde{E}_S}{\tilde{P}_U} + \left(\frac{1}{\tilde{P}_S} - 1 \right) (\tilde{E}_U + \tilde{E}_a) \\ &= \frac{\tilde{E}_a vd [e^\eta (1 - P_R) + P_R]^2 + \pi \kappa^2 \tilde{P}_t \cdot H(\eta, P_R)}{vd (e^\eta - 1) P_R [e^\eta (2 - P_R) + P_R]}\end{aligned}\quad (34)$$

$$H(\eta, P_R) = e^{2\eta} [P_R (4 - 3P_R) + 2\eta (1 - P_R)^2] - 4e^\eta P_R (1 - P_R) - P_R^2 \quad (35)$$

3.2.1 Optimizations

The partial derivative of \tilde{E}_M with respect to d is:

$$\frac{\partial \tilde{E}_M}{\partial d} = \frac{\pi \kappa^2 \tilde{P}_t (4\tau^2 d^2 - \omega^2 - 4\sigma^2) \cdot H(\eta, P_R)}{vd^2 (\omega^2 + 4\sigma^2) (e^\eta - 1) P_R [e^\eta (2 - P_R) + P_R]} \quad (36)$$

where $H(\eta, P_R)$ of Eq. (35) is rearranged as a quadratic equation of P_R :

$$H(\eta, P_R) = \mathcal{H}_1(\eta) P_R^2 - \mathcal{H}_2(\eta) P_R + \mathcal{H}_3(\eta) \quad (37)$$

where $\mathcal{H}_1(\eta) = 2e^{2\eta} (\eta - 1) + 2e^\eta - (e^\eta - 1)^2 > 0$, $\mathcal{H}_2(\eta) = 4e^{2\eta} (\eta - 1) + 4e^\eta > 0$, and $\mathcal{H}_3(\eta) = 2\eta \cdot e^{2\eta}$. The axis of symmetry is $\frac{\mathcal{H}_2(\eta)}{2\mathcal{H}_1(\eta)} > 1$, obtaining:

$$H(\eta, P_R) \geq H(\eta, 1) = e^{2\eta} - 1 > 0 \quad (38)$$

Therefore, the optimum spiral pitch d_{opt} is same with Eq. (21). Analogously, we bring it into Eq. (34) and then get:

$$\tilde{E}_M \Big|_{d=d_{opt}} = \frac{2\pi e^{1/2} \kappa^2 B \sqrt{\omega^2 + 4\sigma^2} \cdot H(\eta, P_R)}{v (e^\eta - 1) P_V [e^\eta (2 - P_R) + P_R]} + \frac{\tilde{E}_a [e^\eta (1 - P_R) + P_R]^2}{(e^\eta - 1) P_R [e^\eta (2 - P_R) + P_R]} \quad (39)$$

The partial derivative of Eq. (39) concerning ω :

$$\frac{\partial \tilde{E}_M}{\partial \omega} = \frac{\omega}{\sqrt{\omega^2 + 4\sigma^2}} \cdot \frac{2\pi e^{1/2} \kappa^2 B \cdot H(\eta, P_R)}{v (e^\eta - 1) P_V [e^\eta (2 - P_R) + P_R]} \quad (40)$$

It can be obtained from Eq. (38) that $\partial \tilde{E}_M / \partial \omega$ greater than zero constantly. Thereby the optimum beam divergence angle ω_{opt} is also equal ω_{limit} .

Meanwhile the partial derivative with respect to τ is:

$$\frac{\partial \tilde{E}_M}{\partial \tau} = \frac{4\pi e^{1/2} \kappa^2 B \sqrt{\omega^2 + 4\sigma^2} P_R^2 \cdot J(\eta, P_R) - 4v \tilde{E}_a e^{2\eta} P_V [e^\eta (1 - P_R) + P_R]}{v (e^\eta - 1) P_R^2 [e^\eta (2 - P_R) + P_R]^2} \quad (41)$$

$$\begin{aligned}J(\eta, P_R) &= e^{3\eta} [(3 - 2\eta) (2 - P_R)^2 + 2\eta - 4] + e^\eta (5P_R - 4) P_R \\ &\quad + e^{2\eta} [P_R^2 (2\eta - 7) + 16P_R - 2\eta - 8] - P_R^2\end{aligned}\quad (42)$$

In addition, the partial derivative of $J(\eta, P_R)$ concerning P_R is:

$$\frac{\partial J(\eta, P_R)}{\partial P_R} = [e^\eta (2 - P_R) + P_R] [e^{2\eta} (2\eta - 3) + 4e^\eta - 1] > 0 \quad (43)$$

It is shown that $J(\eta, P_R)$ is monotonically increasing with respect to P_R , with its maximum value achieved at $P_R = 1$, i.e., $J(\eta, 1) = -(e^{2\eta} - 1)(e^\eta - 1) < 0$. Therefore, $J(\eta, P_R)$ is always less than zero, and $\partial \tilde{E}_M / \partial \tau$ as well. Consequently, the minimum \tilde{E}_M is achieved at $\tau_{opt} = 1/2$.

Furthermore, the partial derivative concerning η is calculated after taking $\tau_{opt} = 1/2$ into Eq. (39) as:

$$\frac{\partial \tilde{E}_M}{\partial \eta} = \frac{4\pi e^{1/2} \kappa^2 B (1 - P_V) e^\eta [e^\eta (1 - P_V) + P_V] \cdot G(\eta, P_V, \hat{E}_a)}{(\omega^2 + 4\sigma^2)^{-1/2} v(e^\eta - 1)^2 P_V [e^\eta (2 - P_V) + P_V]^2} \quad (44)$$

$$G(\eta, P_V, \hat{E}_a) = e^{2\eta} (2 - P_V) - 2e^\eta (\eta - P_V \eta + \hat{E}_a + 1) + P_V \quad (45)$$

The partial derivative of the key term $G(\eta, P_V, \hat{E}_a)$ with respect to η is:

$$\frac{\partial G(\eta, P_V, \hat{E}_a)}{\partial \eta} = 2e^\eta [(2 - P_V)(e^\eta - \eta - 1) + \eta - \hat{E}_a] \quad (46)$$

It can be seen that as η increases, $G(\eta, P_V, \hat{E}_a)$ first decreases and then increases. Since $G(0, P_V, \hat{E}_a) = -2\hat{E}_a < 0$ and $G(\hat{E}_a + 1, P_V, \hat{E}_a) > (2 - P_V)e^\eta(e^\eta - 2\eta) > 0$, $G(\eta, P_V, \hat{E}_a)$ must have a unique zero point corresponding to the minimum \tilde{E}_M . However, it is hard to solve $G(\eta, P_V, \hat{E}_a) = 0$. We employ $x = \ln(\hat{E}_a)$ and P_V as variables and perform polynomials fitting with numerical solutions, with \hat{E}_a and P_V within $[0.01, 10]$ and $[0.1, 1)$, respectively, as well as $Gof = 0.999$. The piecewise fitted polynomials are:

$$\eta_{opt} = \begin{cases} 0.0305x^2 + 0.0115P_Vx + 0.002P_V^2, & 0.01 \leq \hat{E}_a < 0.1 \\ + 0.3279x + 0.0487P_V + 1.01 & \\ 0.0701x^2 + 0.0685P_Vx + 0.0318P_V^2, & 0.1 \leq \hat{E}_a \leq 1 \\ + 0.4678x + 0.1261P_V + 1.147 & \\ 0.0721x^2 + 0.1384P_Vx + 0.1485P_V^2, & 1 < \hat{E}_a \leq 10 \\ + 0.4602x + 0.0057P_V + 1.168 & \end{cases} \quad (47)$$

Thereby $U_{opt} = \kappa \sqrt{2\eta_{opt}}$.

4 Discussion of the results

In this section, MC simulations are conducted to validate the derived analytical expressions. The simulation time step aligns with the sampling interval of the photoelectric sensor. Following the methodology outlined in Ref. Kasdin [1995], random amplitudes and phases are assigned based on the power spectral density of the platform vibration, yielding a frequency-domain sequence. This sequence undergoes inverse Fourier transformation to generate a random time-domain sequence representing platform vibration. This sequence is then superimposed onto the nominal spirals to obtain the simulated scanning trajectory. The simulation process is depicted in Fig. 3, accompanied by the corresponding simulation parameters listed in Table 1.

Fig. 4 shows the variation of the multi-field acquisition energy of (a) scan-stare and (b) dual-scan modes with spiral pitch under different combinations of turbulence, beam divergence angle, and coverage factor, where $U/\kappa = 1.3$. The simulation process is illustrated in Fig. 3. The theoretical values E_M and \tilde{E}_M are calculated according to Eqs. (19) and (34), and the optimum spiral pitch d_{opt} is obtained from Eq. (21). It can be observed that the theoretical results are consistent with the corresponding MC results. When $d < d_{opt}$, the scan time is longer, and while $d > d_{opt}$, the transmitted power that satisfies the received SNR threshold is larger, both of which lead to excessive acquisition energy. In addition, as the beam divergence angle increases and the coverage factor decreases, d_{opt} gradually increases. Meanwhile, the increase of turbulence only increases the acquisition energy without changing d_{opt} . Consequently, the optimization conclusion regarding the spiral pitch is validated. It is observed that the energy of both modes is nearly identical, and relevant quantitative analyses are subsequently conducted.

Fig. 5 shows the variation of (a) acquisition energy and (b) ratio of multi-field scan-stare and dual-scan modes with coverage factor under different field detection probabilities, respectively, where $\omega = 25\mu rad$, $U/\kappa = 1.3$, spiral pitch is

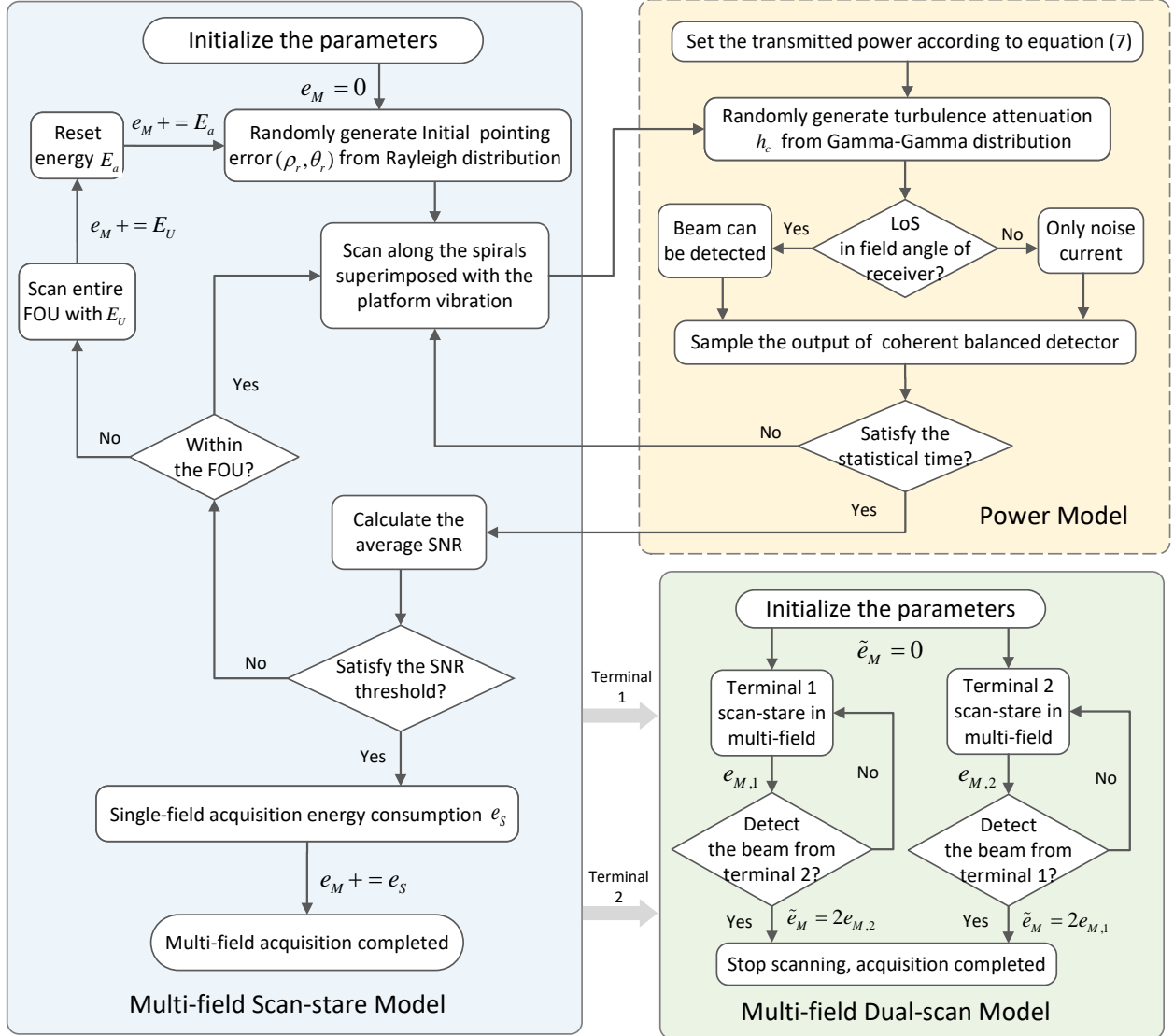


Figure 3: Simulation process of Monto Carlo

calculated from Eq. (21), and the turbulence is medium. The acquisition energy decreases with the increase of coverage factor, and this trend is also reflected in Fig. 4. In addition, an increase in field detection probability P_V means a greater single-field acquisition probability, which can effectively reduce the number of scans without changing the single-field scanning time and reduce the acquisition energy. Therefore, it is advisable to select a photodetector with a larger field angle as much as possible. Observing box plot (b), it is apparent that the median of the ratio is below one, suggesting that the acquisition energy consumption of the dual-scan is statistically lower than that of the scan-stare mode.

Fig. 6 shows the variation of multi-field acquisition energy of (a) scan-stare and (b) dual-scan with FOU under different combinations of turbulence, field detection probability, and reset energy, respectively, where $\omega = 25\mu\text{rad}$, $\tau = 1/2$, and the spiral pitch is calculated from Eq. (21) as $d = 32\mu\text{rad}$. The theoretical optimum FOU U_{opt} for scan-stare and dual-scan modes are fitted by Eq. (27) and (47), respectively. The theoretical results are observed to align well with the corresponding Monte Carlo (MC) results. For small values of U , variations in reset energy significantly affect acquisition energy consumption. At $U/\kappa = 0.4$, the acquisition energy consumption of $E_a = 3$ increases by 38% compared to that of $E_a = 1$. Conversely, for large values such as $U/\kappa = 2.5$, the acquisition energy consumption of $E_a = 3$ increases by only 0.1% compared to that of $E_a = 1$. In this case, the impact of reset energy variation can be neglected, and scanning energy consumption plays a dominant role. This is because with the increase of FOU, the

Table 1: Simulation parameters

Parameters	Value	Unit
Link distance R	36000	km
Transmitter loss s_t	0.92	-
Receiver loss s_r	0.92	-
Receiver aperture diameter D_r	30	cm
Proportion of split beam s_s	0.1	-
Photoelectric response efficiency R_r	0.88	-
Std. of noise current σ_n	8	nA
Local oscillator power P_L	0.1	mW
Receiver average SNR threshold \bar{Q}	10	dB
Statistical time for average SNR	1	s
Band-limited platform vibration	100	Hz
Sample frequency of photodetector	10	KHz
Weak turbulence scale γ	0.9	-
Medium turbulence scale γ	0.5	-
Std. of platform vibration σ	10	μrad
Std. of initial LOS error κ	1	$mrad$
Scanning speed v	10	$\mu rad/s$
Reset energy E_a	1	J
Field detection probability P_V	0.95	-

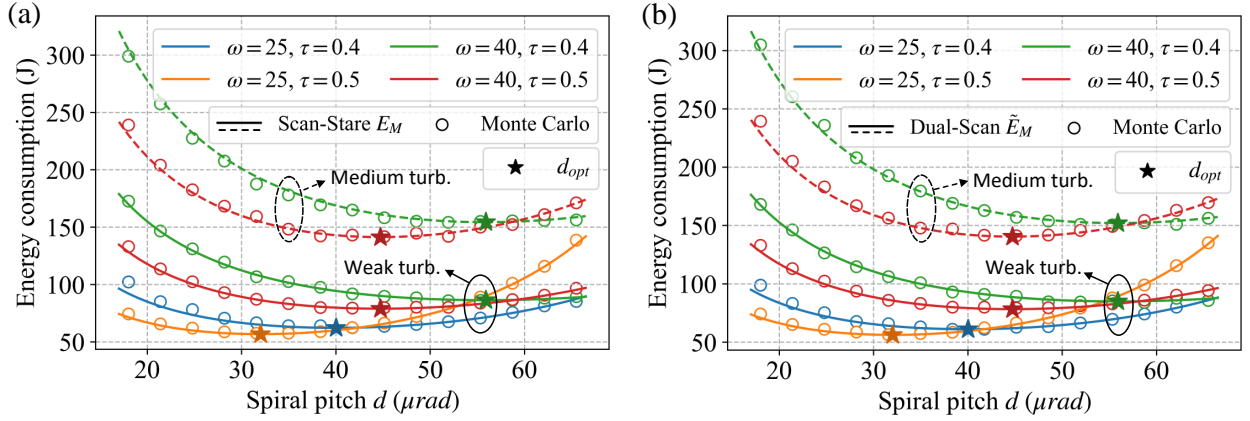


Figure 4: The variation of the multi-field acquisition energy with spiral pitch under different combinations of turbulence, beam divergence angle, and coverage factor. (a) scan-stare and (b) dual-scan.

single-field acquisition probability increases, and the scanning time decrease, leading to a decrease in total reset energy. On the other hand, the energy for scanning the entire FOU E_U or \tilde{E}_U is proportional to the square of U , which is a high-order term compared to E_a . In addition, when $U > U_{opt}$, the acquisition energy almost does not change with the variation of FOU in the case of $P_V = 0.99$. Theoretically, when $P_R = P_{SNR}P_V = 0.99 \rightarrow 1$, the acquisition energy for scan-stare and dual-scan are $E_M \rightarrow 2\pi\kappa^2 P_t/(vd)$ and $\tilde{E}_M \rightarrow \pi\kappa^2 \tilde{P}_t/(vd)$, respectively, which are not related to FOU. This means that the selection of FOU can be more flexible. Meanwhile, increasing E_a and P_V or decreasing turbulence leads to an increase in U_{opt} . Furthermore, the difference between the fitted U_{opt} and the corresponding acquisition energy of scan-stare and dual-scan with the ground-truth values are within 1% and $10^{-3}\%$ as well as within 1% and $10^{-2}\%$, respectively, validating the optimization conclusion about FOU.

Through the above quantitative analysis, it can be inferred that under the same parameters, the multi-field acquisition energy consumption of both modes is almost identical. Consequently, Fig. 7 examines the variation of platform vibration at different scanning speeds in the more complex dual-scan mode, where $\omega = 25\mu rad$, $d = 30\mu rad$, $\tau = 1/2$, $U/\kappa = 1.3$, and the turbulence is medium. To maintain a consistent scan length for average SNR statistics, the duration of the statistical time is set as follows: 1 second for $v = 10\mu rad$, 0.5 seconds for $v = 20\mu rad$, 0.25 seconds for

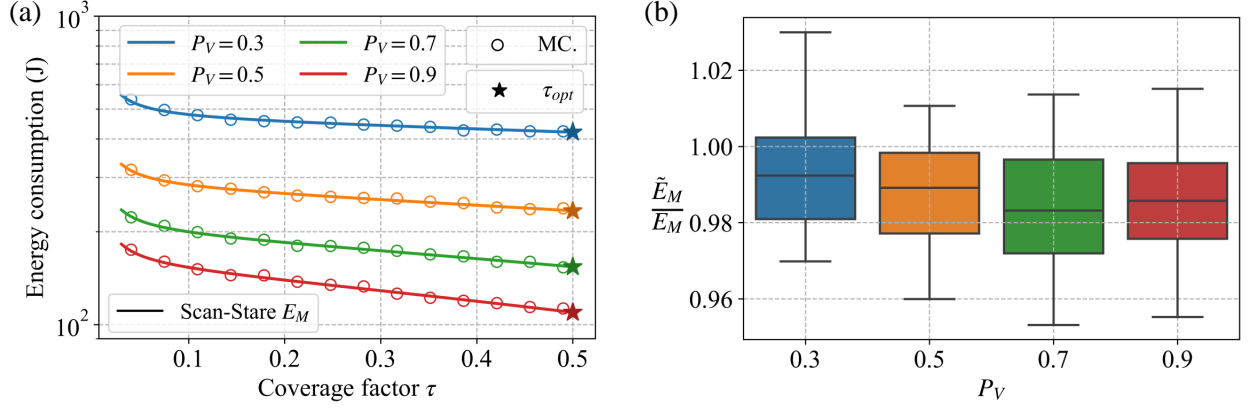


Figure 5: The results under different field detection probabilities vary with the coverage factor. (a) Multi-field acquisition energy for scan-stare. (b) Ratio of energy consumption between dual-scan and scan-stare modes.

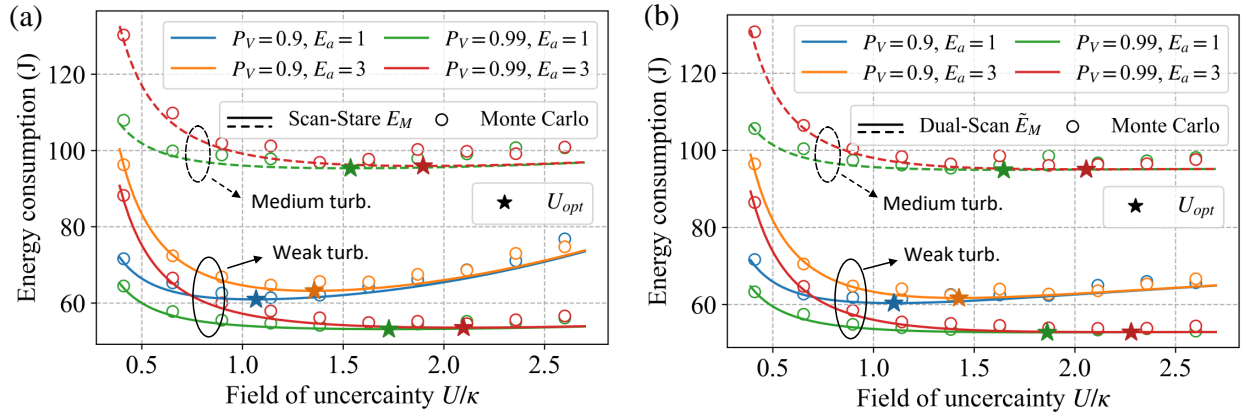


Figure 6: The variation of multi-field acquisition energy with FOU under different combinations of turbulence, field detection probability, and reset energy. (a) scan-stare. (b) dual-scan.

$v = 40\mu rad$, and 0.125 seconds for $v = 80\mu rad$. In Fig. 7 (a), it is evident that as the platform vibration intensity increases, the acquisition energy consumption gradually rises. This is because the power required at the transmitter increases to meet the SNR threshold at the receiver. Moreover, maintaining the same scan length at different speeds ensures consistent expectations for statistically averaged SNR. However, increasing the vibration intensity and reducing the SNR statistical time lead to increased variance, resulting in a flatter probability density curve. Consequently, this results in a decrease in the probability of the average SNR exceeding the threshold, as depicted in Fig. 7 (b), leading to a decline in single-field acquisition probability and causing the simulated energy consumption to deviate further from the theoretical value illustrated in Fig. 7 (a). Notably, the consistency between simulation and theory is highest at $v = 10\mu rad$.

Subsequently, Fig. 8 presents simulation on the variation of scanning speed under different spiral pitches, where $\omega = 25\mu rad$, $\tau = 1/2$, $U/k = 1.3$, and the turbulence is medium. In Fig. 8 (a), as the scanning speed increases, the scanning time decreases, leading to a reduction in multi-field acquisition energy consumption. Additionally, the simulated energy consumption gradually deviates from the theoretical value as the scanning speed increases. This is because the increased scanning length within the 1-second period for average SNR statistics causes some trajectory points to be significantly farther from the receiver, resulting in a significant decrease in received power and consequently reducing the average SNR at the receiver, as shown in Fig. 8 (b), causing a decrease in single-field acquisition probability. Moreover, in Fig. 8 (b), the P_{SNR} located on the curve of $d = 30\mu rad$ corresponding to $v = 10\mu rad$ is 0.992, which is annotated with a black dashed line. Subsequently, the speeds on the curves for $d = 50\mu rad$ and $d = 70\mu rad$, where the consistency between simulation and theory is 99.2%, are recorded as $16.9\mu rad/s$ and $23.2\mu rad/s$, respectively. Given

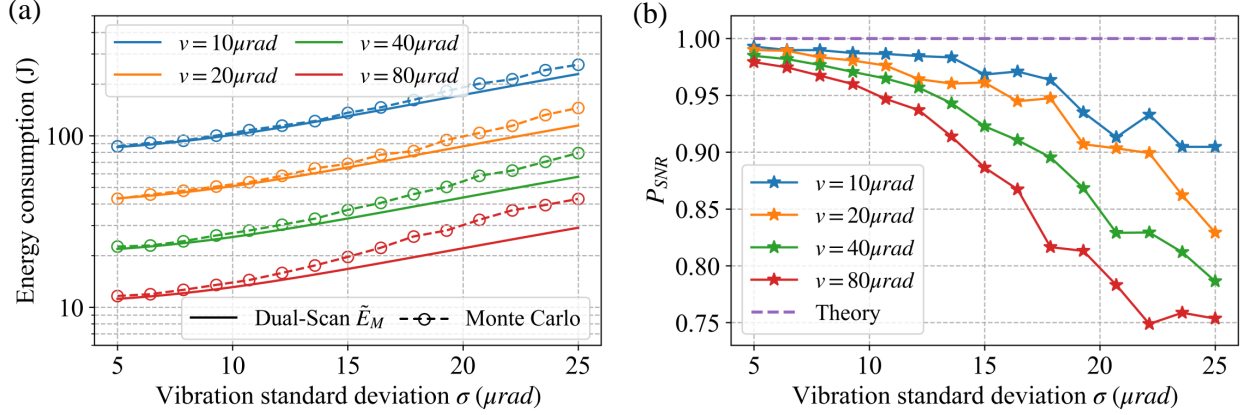


Figure 7: The results of dual-scan under different scanning speeds as the platform vibration increases. (a) Multi-field acquisition energy consumption plotted on a logarithmic scale. (b) Probability of average SNR exceeding the threshold.

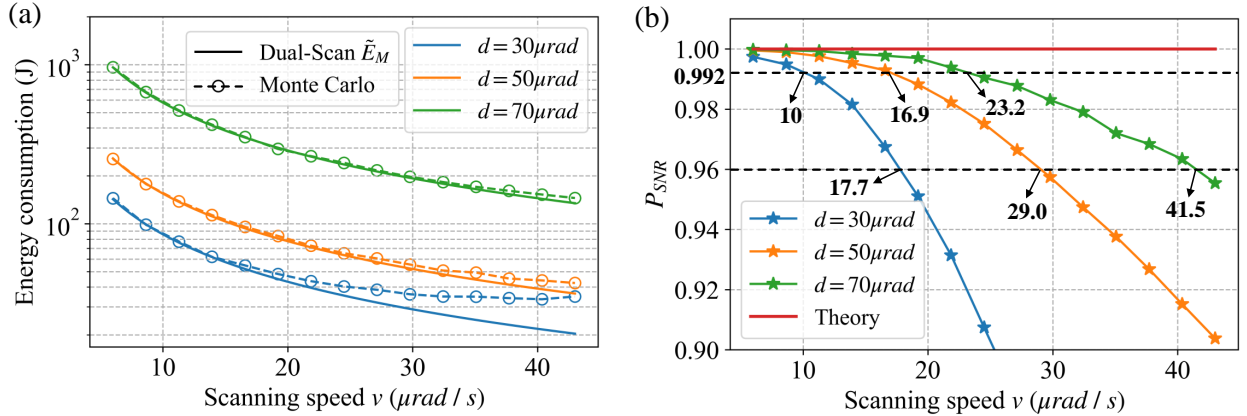


Figure 8: The results for dual-scan under different spiral pitches as the scanning speed changes. (a) Multi-field acquisition energy consumption plotted on a logarithmic scale. (b) Probability of average SNR over the threshold.

that the maximum acquisition angles τd satisfying the SNR threshold for three spiral pitches are $15\mu\text{rad}$, $25\mu\text{rad}$, and $35\mu\text{rad}$, respectively, the ratios of scanning length within the 1-second statistical time to maximum acquisition angle (denoted as ε) are calculated as 0.67, 0.68, and 0.66, respectively, indicating their close proximity. To validate this quantitative relationship, the speeds where the consistency between simulation and theory is 96% on three spiral pitches are identified as $17.7\mu\text{rad}/s$, $29.0\mu\text{rad}/s$, and $41.5\mu\text{rad}/s$, respectively, then the corresponding ε are 1.18, 1.16, and 1.19, respectively, demonstrating their close proximity. Furthermore, the simulation consistencies corresponding to different ε are listed in Table 2. It is apparent that to hold good simulation consistency, the selection of ε should be less than one.

Finally, Fig. 9 describes the changes in multi-field acquisition energy consumption for two modes with increasing beam divergence angle, where the turbulence is medium, $U/\kappa = 1.3$, $d = 30\mu\text{rad}$, $\tau = 1/2$, and $v = 10\mu\text{rad}/s$ to hold 99% simulation consistency. The corresponding acquisition time is also plotted in Fig. 9. It is evident that the energy curves of the two modes almost overlap. Moreover, as ω increases, although the acquisition time decreases, the energy increases. This is because the transmitted power required increases significantly to guarantee that the received average SNR is greater than the threshold. In particular, the typical divergence angle of the beaconless is about $10 \sim 50\mu\text{rad}$, highlighted in the orange region, and the average acquisition energy is $107J$. While the divergence angle of the beacon is typically $10 \sim 30$ times greater than the beaconless, shown as the red region, and the average acquisition energy is $1881J$, which is about 18 times greater than that of the beaconless. Furthermore, the minimum energy consumption is achieved at minimum beam divergence angle ω_{limit} , which is also the divergence angle during the APT tracking

Table 2: The Relationship between ε and Simulation Consistency

The ratio ε	Simulation Consistency (%)
0.5	99.63
1	97.64
1.5	92.6
2	85.3
2.5	75.88
3	63.86

ε is the ratio of scan length within the time for average SNR statistics to maximum acquisition angle.

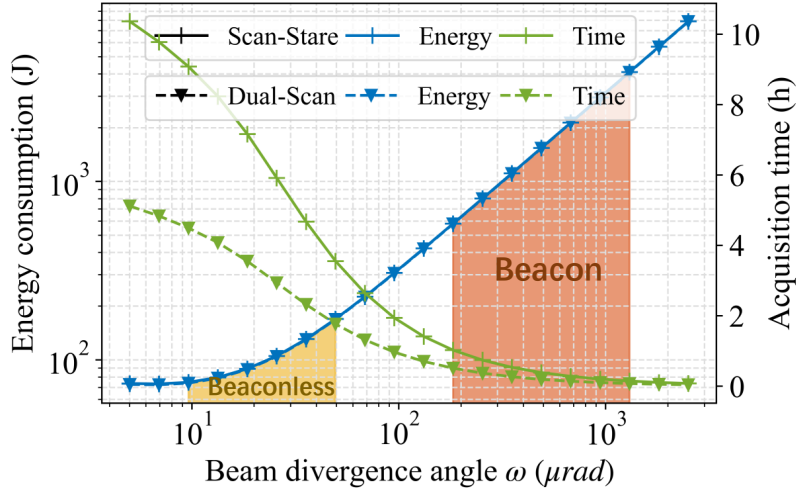


Figure 9: The variations of acquisition energy consumption and time with the beam divergence angle. The beaconless and the beacon are represented with orange and red regions, respectively.

phase. This quantitatively concludes that the beaconless is superior to the beacon for APT with the goal of minimizing energy consumption. Given that the acquisition time of the dual-scan is about half that of the scan-stare, thus the former outperforms the latter in terms of acquisition efficiency.

5 Conclusion

This paper conducts a detailed and comprehensive study of energy consumption, an important resource for the satellite to execute missions, based on the received average SNR with multi-field scanning for GEO-to-ground optical link acquisition. We first establish a link model from transmitted power to received SNR under the coherent detection system, involving factors such as turbulence, platform vibration, beam divergence angle, spiral pitch, coverage factor, as well as various losses. This model is applicable to various photodetectors, thus holding practical guidance significance. Combined with the acquisition time and the essential reset energy preparing for the next single-field scanning, we derive the closed-form expression of multi-field acquisition energy and perform optimization in the scan-stare mode. Subsequently, we discuss another mode called the dual-scan, where two terminals synchronously scan until one acquires the other. Through simulations, we find that the acquisition energy of the dual-scan is lower than that of scan-stare. Meanwhile, the acquisition time of the former is about half of the latter, which further enhances the advantage of dual-scan in acquisition efficiency. Moreover, simulation results regarding platform vibration and scanning speed variations indicate that when the ratio of scan length within the time for average SNR statistics to maximum acquisition angle is less than one, the consistency between the theoretical model and simulation results exceeds 97%. Notably, the proposed model can be extended to optical link acquisition scenarios between satellites in the same orbit due to the consideration of turbulence effects. Finally, we compare the acquisition energy of the beaconless and the beacon in their typical range, and observe that the energy consumption with beaconless is only 6% of that with beacon, indicating that the beaconless is a better strategy for optical link acquisition with the goal of energy optimization, providing strong theoretical support for FSOC system miniaturization.

Disclosures

The authors declare no conflicts of interest.

References

- Morio Toyoshima, Walter R Leeb, Hiroo Kunimori, and Tadashi Takano. Comparison of microwave and light wave communication systems in space applications. *Optical engineering*, 46(1):015003–015003, 2007.
- Morio Toyoshima. Trends in satellite communications and the role of optical free-space communications. *Journal of Optical Networking*, 4(6):300–311, 2005.
- Isaac I Kim, Brian Riley, Nicholas M Wong, Mary Mitchell, Wesley Brown, Harel Hakakha, Prasanna Adhikari, and Eric J Korevaar. Lessons learned for strv-2 satellite-to-ground lasercom experiment. In *Free-Space Laser Communication Technologies XIII*, volume 4272, pages 1–15. SPIE, 2001.
- Renny Fields, David Kozlowski, Harold Yura, Robert Wong, Josef Wicker, C Lunde, Mark Gregory, B Wandernoth, and F Heine. 5.625 gbps bidirectional laser communications measurements between the nfire satellite and an optical ground station. In *2011 International Conference on Space Optical Systems and Applications (ICSOS)*, pages 44–53. IEEE, 2011.
- Edoardo Benzi, Daniel C Troendle, Ian Shurmer, Mark James, Michael Lutzer, and Sven Kuhlmann. Optical inter-satellite communication: the alphasat and sentinel-1a in-orbit experience. In *14th International Conference on Space Operations*, page 2389, 2016.
- Harald Hauschildt, Nicolas le Gallou, Silvia Mezzasoma, Hermann Ludwig Moeller, Josep Perdigues Armengol, Michael Witting, Jörg Herrmann, and Cesar Carmona. Global quasi-real-time-services back to europe: Edrs global. In *International Conference on Space Optics—ICSO 2018*, volume 11180, pages 353–357. SPIE, 2019.
- Philip W Young, Lawrence M Germann, and Roy Nelson. Pointing, acquisition, and tracking subsystem for space-based laser communications. In *Optical technologies for communication satellite applications*, volume 616, pages 118–128. SPIE, 1986.
- Danielle MR Wuchenich, Christoph Mahrtdt, Benjamin S Sheard, Samuel P Francis, Robert E Spero, John Miller, Conor M Mow-Lowry, Robert L Ward, William M Klipstein, Gerhard Heinzl, et al. Laser link acquisition demonstration for the grace follow-on mission. *Optics express*, 22(9):11351–11366, 2014.
- Enrico Barausse, Emanuele Berti, Thomas Hertog, Scott A Hughes, Philippe Jetzer, Paolo Pani, Thomas P Sotiriou, Nicola Tamanini, Helvi Witek, Kent Yagi, et al. Prospects for fundamental physics with lisa. *General Relativity and Gravitation*, 52:1–33, 2020.
- Ziren Luo, Yan Wang, Yueliang Wu, Wenrui Hu, and Gang Jin. The taiji program: A concise overview. *Progress of Theoretical and Experimental Physics*, 2021(5):05A108, 2021.
- M Guelman, Anton Kogan, A Kazarian, A Livne, M Orenstein, and H Michalik. Acquisition and pointing control for inter-satellite laser communications. *IEEE Transactions on Aerospace and Electronic Systems*, 40(4):1239–1248, 2004.
- Morio Toyoshima, Takashi Jono, Keizo Nakagawa, and Akio Yamamoto. Optimum divergence angle of a gaussian beam wave in the presence of random jitter in free-space laser communication systems. *JOSA A*, 19(3):567–571, 2002.
- Hugo Steinhaus. *Mathematical snapshots*. Courier Corporation, 1999.
- Sen Yang and Xiaofeng Li. Derivation of ambiguity in wavefront aberration and quantitative analysis in ao system. *Optics and Lasers in Engineering*, 158:107174, 2022a.
- Sen Yang and Xiaofeng Li. Iterative framework for a high accuracy aberration estimation with one-shot wavefront sensing. *Optics Express*, 30(21):37874–37887, 2022b.
- Wujie Fu, Shaokang Chen, Jian Guan, Zhongtan Zhang, Hao Wu, and Dong F Wang. A virtual-movement scheme for eliminating spot-positioning errors applicable to quadrant detectors. *IEEE Transactions on Instrumentation and Measurement*, 70:1–11, 2021.
- Zhaobing Qiu, Liyu Lin, and Liqiong Chen. An active method to improve the measurement accuracy of four-quadrant detector. *Optics and Lasers in Engineering*, 146:106718, 2021.
- Siyuan Yu, Feng Wu, Qiang Wang, Liying Tan, and Jing Ma. Theoretical analysis and experimental study of constraint boundary conditions for acquiring the beacon in satellite–ground laser communications. *Optics Communications*, 402:585–592, 2017.

- Siqi Hu, Hanghua Yu, Zheng Duan, Ye Zhu, Caixia Cao, Miaomiao Zhou, Guotong Li, and Huijie Liu. Multi-parameter influenced acquisition model with an in-orbit jitter for inter-satellite laser communication of the Ices system. *Optics Express*, 30(19):34362–34377, 2022.
- Charles Hindman and Lawrence Robertson. Beaconless satellite laser acquisition-modeling and feasibility. In *IEEE MILCOM 2004. Military Communications Conference, 2004.*, volume 1, pages 41–47. IEEE, 2004.
- Tzung-Hsien Ho. *Pointing, acquisition, and tracking systems for free-space optical communication links*. University of Maryland, College Park, 2007.
- Xin Li, Siyuan Yu, Jing Ma, and Liying Tan. Analytical expression and optimization of spatial acquisition for intersatellite optical communications. *Optics Express*, 19(3):2381–2390, 2011.
- Lothar Friederichs, Uwe Sterr, and Daniel Dallmann. Vibration influence on hit probability during beaconless spatial acquisition. *Journal of Lightwave Technology*, 34(10):2500–2509, 2016.
- Jing Ma, Gaoyuan Lu, Liying Tan, Siyuan Yu, Yulong Fu, and Fajun Li. Satellite platform vibration influence on acquisition system for intersatellite optical communications. *Optics & Laser Technology*, 138:106874, 2021.
- Gerald Hechenblaikner. Analysis of performance and robustness against jitter of various search methods for acquiring optical links in space. *Applied Optics*, 60(13):3936–3946, 2021.
- Hemani Kaushal and Georges Kaddoum. Optical communication in space: Challenges and mitigation techniques. *IEEE communications surveys & tutorials*, 19(1):57–96, 2016.
- Hanshan Li. Limited magnitude calculation method and optics detection performance in a photoelectric tracking system. *Applied Optics*, 54(7):1612–1617, 2015.
- Keith B Chin, Erik J Brandon, Ratnakumar V Bugga, Marshall C Smart, Simon C Jones, Frederick C Krause, William C West, and Gary G Bolotin. Energy storage technologies for small satellite applications. *Proceedings of the IEEE*, 106(3):419–428, 2018.
- Huanxi Cui, Lipeng Zhu, Zhenyu Xiao, Bruno Clerckx, and Rui Zhang. Energy-efficient rsma for multigroup multicast and multibeam satellite communications. *IEEE Wireless Communications Letters*, 2023.
- Larry C Andrews and Ronald L Phillips. Laser beam propagation through random media. *Laser Beam Propagation Through Random Media: Second Edition*, 2005.
- Wasiu O Popoola, Enrique Poves, and Harald Haas. Spatial pulse position modulation for optical communications. *Journal of Lightwave Technology*, 30(18):2948–2954, 2012.
- Kostas P Peppas and P Takis Mathiopoulos. Free-space optical communication with spatial modulation and coherent detection over hk atmospheric turbulence channels. *Journal of Lightwave Technology*, 33(20):4221–4232, 2015.
- Antonio Jurado-Navas, José María Garrido-Balsells, José Francisco Paris, Miguel Castillo-Vázquez, and Antonio Puerta-Notario. Impact of pointing errors on the performance of generalized atmospheric optical channels. *Optics Express*, 20(11):12550–12562, 2012.
- Ammar Al-Habash, Larry C Andrews, and Ronald L Phillips. Mathematical model for the irradiance probability density function of a laser beam propagating through turbulent media. *Optical engineering*, 40(8):1554–1562, 2001.
- Ning Wang and Julian Cheng. Moment-based estimation for the shape parameters of the gamma-gamma atmospheric turbulence model. *Optics express*, 18(12):12824–12831, 2010.
- Aleš Prokeš. Modeling of atmospheric turbulence effect on terrestrial fso link. *Radioengineering*, 18(1):42–47, 2009.
- N Jeremy Kasdin. Discrete simulation of colored noise and stochastic processes and 1/f/sup/spl alpha//power law noise generation. *Proceedings of the IEEE*, 83(5):802–827, 1995.